ADVANCED ENGINEERING MATERIALS

DOI: 10.1002/adem.201600675

Deformation-Induced Supersaturation in Immiscible Material Systems during High-Pressure Torsion**

By *Karoline Sophie Kormout, Reinhard Pippan* and *Andrea Bachmaier**

The review focuses on the supersaturation process of immiscible elements induced by high-pressure torsion deformation. A variety of investigated material systems offers the systematic analysis of the controlling factors for mechanical intermixing, which are mainly determined by the level of the positive heat of mixing and the deformation behavior. The homogeneity of the deformation process strongly influences the degree of supersaturation. Our results show that the fundamental mixing mechanism during deformation is not necessarily the same in all systems, but depends also on the strength differences of the phases and accordingly the deformation behavior.

1. Introduction

The first observations of mechanical alloying or deformation-induced mixing were made in ball milling experiments more than 20 years ago. Extended solubilities or complete supersaturation was achieved in many material systems, such as Cu–Cr,[1] Cu–W,[2] Cu–Co,[3] Cu–Ag,[4–6] Ni–Ag,[7] Cu–Fe,[8–11] or Ag–Fe.[12] A review on mechanical alloying can be found in ref.[13] Since Li et al.[14] provided evidence that the dissolution of cementite and consequential supersaturation of carbon in ferrite in perlitic steel wires led to extraordinary high strength, the phenomenon of deformation-induced mixing in usually immiscible systems has regained increased attention to the materials science community. Composites of immiscible elements stand out due to the very high structural and thermal stability compared to single-phase alloys. For instance, developments in the mechanical and electrical properties of Cu-based composites proceed for applications in robotics and high-pulse field magnets.[15–19] Moreover, it is possible to tune magnetic properties by alloying or decomposition. Cu–Fe nanocomposites with small amounts of Cu are expected to have large magnetostrictive effects,[20,21] and Cu–Co alloys with nano-sized Co precipitates in a Cu matrix are considered to exhibit a giant magnetoresistance effect.[22,23]

Severe plastic deformation (SPD) techniques like, for example, high-pressure torsion (HPT) deformation, and accumulative roll bonding (ARB), enable the production of composites with ultra-fine grained (UFG), or nanocrystalline (NC) microstructures. In addition, supersaturated solid solution formation, as well as amorphization reactions have been observed in several studies independent of the used SPD method.[24–36] Microstructure and properties can be tailored for specific applications by combining suitable process parameters with intermediate or post-deformation heat treatments. However, to optimize the properties of composite materials, the required SPD production steps to generate the desired material need to be known. Thus, the deformation behavior and deformation-induced supersaturation or amorphization processes should be understood in detail. This review focuses only HPT deformation, which is a widely used process nowadays. Whereas, ARB has its advantage in the easy up-scaling, the HPT technique allows deformation under high hydrostatic pressure and, therefore, enables the processing of a tremendous number of materials to very high strains without fracture of the sample. Due to the possibility to easily change processing

[*] *Dr. A. Bachmaier, Dr. K. S. Kormout, Prof. R. Pippan*
Erich Schmid Institute of Materials Science, Austrian Academy of Sciences, Jahnstraße 12, 8700 Leoben, Austria
E-mail: andrea.bachmaier@oeaw.ac.at

[**] *Funding of this work has been provided by the European Research Council under ERC Grant Agreement No. 340185 USMS and by the Austrian Science Fund (FWF): J3468-N20.*

A. Bachmaier studied materials science and is currently doing her Post-doc at the Erich Schmid Institute, Austria.

parameters, such as deformation temperature, pressure, strain rate and applied strain the HPT deformation is a convenient technique to link microstructural changes with the deformation-induced mixing process of the constituent phases of the composites and several studies have addressed these issues during HPT.[30–36]

Despite the large number of studies, the underlying deformation-induced mixing processes and the critical factors defining the maximum solubility are still under debate.[33,37–39] Several studies indicate a strong link between the heat of mixing and the degree of supersaturation. In systems with low positive heat of mixing, as for example, Cu–Ag, complete solid solutions are easily reached over the whole composition range during ball milling.[4] In contrast, in systems with high positive heat of mixing, such as Ni–Ag or Ag–Fe, only extended solubilities could be obtained.[7,12,40] Besides thermodynamic considerations, it is proposed that large differences in strength of the individual phases of the composites can lead to strong strain localization, thereby, impeding to achieve full supersaturation during deformation.[41] Since dislocations play a key role in the kinetic roughening model and the dislocation shuffling process, which are proposed to be mechanisms for deformation-induced mixing, the crystal structures of the present phases might additionally influence the amount of mixing.[39,42]

The aim of this paper is to summarize our results on deformation-induced supersaturation, which is observed during HPT processing at room temperature (RT) of several immiscible binary systems. This includes the Ni–Ag (fcc/fcc), Cu–W, Cu–Cr (fcc/bcc), and Cu–Co (fcc/hcp) systems, which have varying crystal structures and strength differences. Additionally, the combination of ductile metals, such as Cu–Ag (fcc/fcc) and Cu–Fe (fcc/bcc) are investigated. All systems have a positive heat of mixing and possess no intermetallic phases. The investigated composites are listed in Table 1 providing information about initial crystal structure, second phase content in at% and vol%, and the achieved microhardness and grain size after deformation. The article is divided in the following chapters: First, the differences between HPT processing of single-phase and composite materials are outlined. Second, the HPT technique is described, including a two-step HPT process, which is especially important for the deformation of coarse composites. Then, the microstructural evolution and its influence on the formation of supersaturated solid solutions in the aforementioned material systems is summarized. The proposed mixing mechanisms and the different factors, which influence deformation-induced mixing, are described in the following. Finally, the enhanced thermal stability of the HPT deformed composite materials is shortly discussed.

2. Differences in Deformation of Single-Phase and Composite Materials

The deformation of pure metals and single-phase alloys by SPD has been investigated intensively in the last two decades and a fundamental understanding of the formation of UFG or NC structures during SPD processing has been provided. During the HPT process, a huge number of dislocations are accumulated. With ongoing deformation, these dislocations arrange to new grain

Table 1. Summary of initial crystal structure, compositions in at% and vol%, Vickers microhardness and grain size in the saturation regime of HPT deformation for the investigated composites.

	at%/vol%	Vickers microhardness in saturation [−]	Grain size in saturation [nm]
Cu–Ag (fcc-fcc)[53,54]	Cu-6/9Ag	≈355	≈30–50 nm
	Cu-16/22Ag	≈380	≈20–40 nm
	Cu-37/46Ag	≈340	≈10 nm
	Cu-26/25Co	≈280	≈100 nm
Cu–Co (fcc-hcp)[55–58]	Cu-54/50Co	≈400	<50 nm
	Cu-76/75Co	≈450	<50 nm
	Cu-17/17Fe	≈330	<50 nm
Cu–Fe (fcc-bcc)[49]	Cu-53/53Fe	≈440	<50 nm
	Cu-73/73Fe	≈445	<50 nm
	Cu-87/87Fe	≈640	<50 nm
Cu–Cr (fcc-bcc)[32,59]	Cu-47/47Cr	≈450	≈10–20 nm
	Ni-6/9Ag	≈700	≈30–50 nm
Ni–Ag (fcc-fcc)[60]	Ni-19/26Ag	≈600	≈10–20 nm
	Ni-35/46Ag	≈480	UFG + NC
	Ni-69/77Ag	≈240	UFG + NC
Cu–W (fcc-bcc)[61–63]	Cu-51/58W	≈550	≈5–15 nm

ADVANCED ENGINEERING MATERIALS

boundaries, which subdivide the initial grains and finally transform the material into an UFG structure.[43] A steady state or saturation regime is then reached, in which microstructural features and hardness are at a constant level, for a detailed review the reader is referred to reference.[43] In the saturation regime, an equilibrium between grain refinement and restoration processes arises. Renk et al.[44] supposed grain boundary motion to be the prevailing recovery mechanism to maintain the microstructure. In pure metals, the saturation microstructure is independent of the initial state of the material. For example, the same saturation microstructure was obtained for single-crystalline, poly-crystalline coarse-grained and electrodeposited NC Ni by HPT deformation.[45,46] The saturation grain size and consequently the saturation hardness of pure metals in HPT can be mainly varied by the deformation temperature and alloying elements or impurities.[43,47] To a minor degree, the strain rate and applied pressure has also an influence.[48]

During deformation of composites, similar grain refinement processes are observed in the beginning of the deformation process within the respective phases. This is valid for phase dimensions in the micrometer range. In single-phase materials relatively low applied strains (about $\varepsilon \approx 20$) are usually sufficient to reach saturation. In composites, however, much higher applied strains are needed due to complex fragmentation processes, if a saturation is ever reached at all by reasonable amounts of applied strains. To increase the effectiveness of composite processing, Bachmaier et al.[49] developed a two-step HPT process. Further details of the two-step process are given in the next chapter.

Different to pure metals or single-phase alloys, the initial arrangement of phases plays a key role in composites, because geometrical changes of the phases dominate the microstructural evolution and the deformation behavior. The volume fraction and mechanical properties (hardness, yield strength, and strain hardening capability) of the constituent phases determine if co-deformation or predominant fracture of hard phases and localized plastic deformation of soft phases are the dominating deformation processes. Moreover, alloying and subsequent supersaturation of individual phases, together with possible amorphization, can lead to further hardening or softening,[32] resulting in a very complex deformation behavior. Additionally, as outlined by Bachmaier et al.,[50] the strain path is important.

3. HPT Deformation Process

Nowadays a quasi-constrained HPT setup is widely used. As shown schematically in Figure 1a, two anvils with cavities, in which a disk-shaped sample is placed, are loaded under high pressure and rotated with respect to another. These cavities allow on the one hand a centering of the sample for accurate torsional straining, and on the other hand a nearly hydrostatic pressure. The used setup has been described in detail in ref.[51] The deformation can be considered as simple shear and the applied strain γ can be evaluated as:[52]

$$\gamma = \frac{2\pi r}{t} n,$$

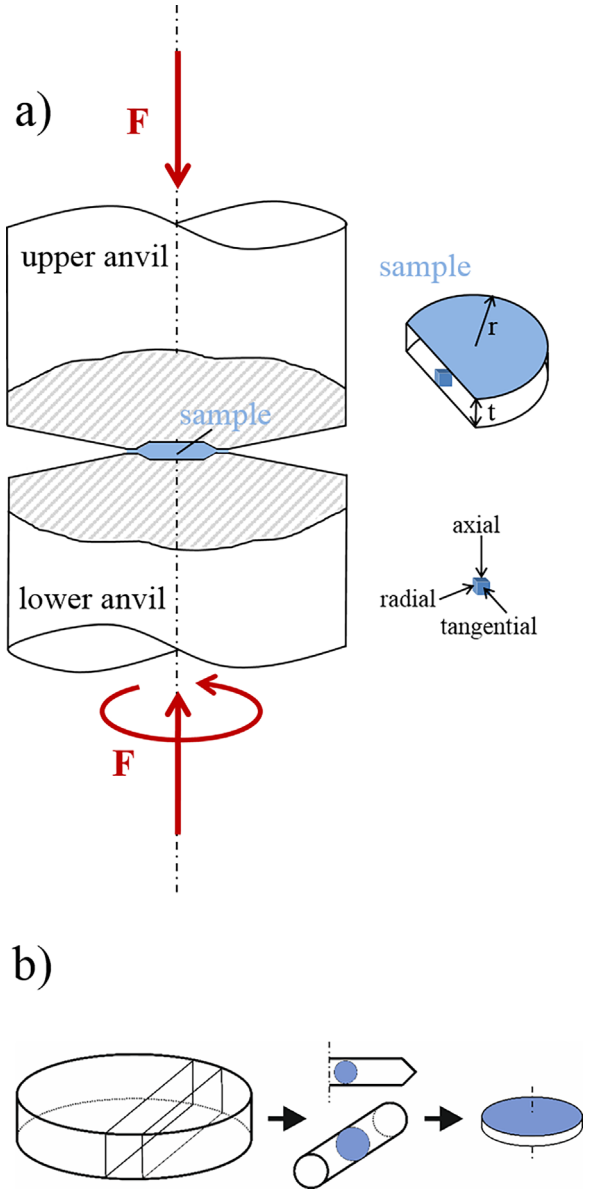

Fig. 1. (a) Schematic of the HPT process. (b) Schematic of the sample preparation procedure for the two-step HPT process.

with the radius r and the thickness t of the sample and the number of rotations n. This is only valid, if no thickness changes occur. The equivalent plastic strain can be calculated with a von Mises equivalent strain as:

$$\varepsilon = \frac{\gamma}{\sqrt{3}}$$

Due to the large miscibility gap in the investigated immiscible systems, a production route via conventional casting techniques is problematic. Therefore, one of the main challenges is to receive bulk starting materials. To overcome this problem, a production route via powders was established. Thereby, almost unlimited material combinations can be produced by blending of elemental powders, which are either pre-compacted using inductive hot pressing or directly compacted in the HPT tool and subsequently deformed.

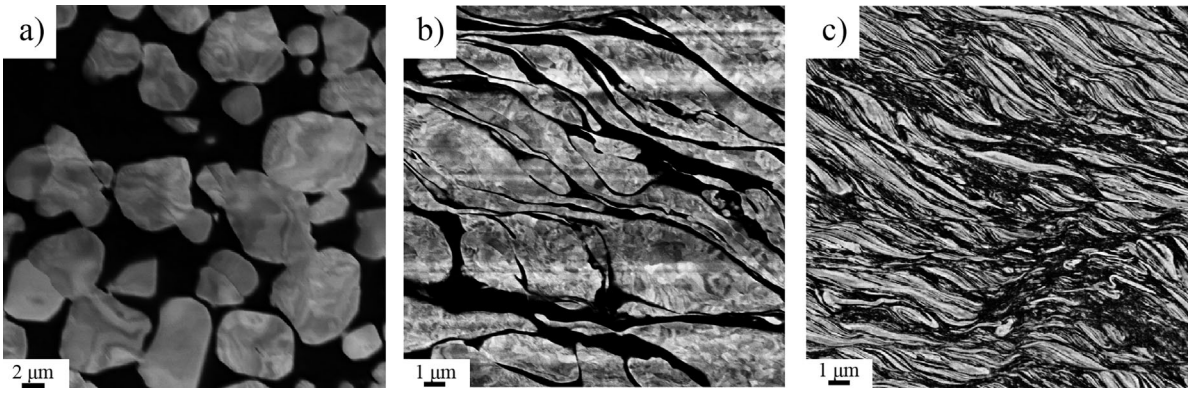

Fig. 2. BSE-SEM micrographs of Cu-51 at% W. (a) For the undeformed bulk material with equi-axed W particles (bright contrast) embedded in the Cu matrix. (b) At an applied strain of $\varepsilon \approx 16$ revealing slight elongation of the W phase und the formation of substructures inside the W particles. (c) At $\varepsilon \approx 64$ strong elongation and fracturing of the W phase occurs leading to fine-dispersed W phase in the Cu phase.

In order to accelerate the size reduction of phase elements, a two-step HPT process is feasible. For this purpose, the powder blends or the initial composite material is first processed in a large HPT tool to obtain a sample with a diameter between 30 and 50 mm and thicknesses up to 10 mm. Afterwards, a cylindrical rod is fabricated out of the sample (see schematic in Figure 1b). From this rod, new small disks are cut and deformed with a smaller HPT tool. The new samples have typical diameters between 6 and 8 mm and thicknesses up to 1 mm. By this process, the shear direction of the second HPT step is rotated by 90° in respect to the first HPT step. Thus, the alignment of the structural elements of the different phases of the composites from the first step is perpendicular to the shear direction in the second step. This increases the effectiveness of the HPT deformation enormously, but only in case ideal co-deformation occurs. However, as discussed in detail in the next section, this is not the case in many immiscible material systems.

4. Deformation of Immiscible Binary Systems

4.1. Fcc-Bcc

The starting composite material has usually a structural size in the micrometer range, as shown for example, for Cu–51 at% W (Figure 2a). The nearly equi-axed W particles appear bright in the backscatter-electron (BSE) scanning electron microscope (SEM) images and are homogeneously distributed in the Cu matrix. Both phases are existent in similar volume fractions (see Table 1). After applying a shear strain of $\varepsilon \approx 16$, the W particles are elongated in shearing direction and fracture of few particles is observed (Figure 2b). Inside the particles, substructures are formed by dislocation accumulation and arrangement, as described in detail for pure metals.[43] Increasing the strain to $\varepsilon \approx 64$ leads to heavy elongation of the W particles and additional refinement in some regions by repeated fractures, which generates very small W fragments distributed in the Cu phase (Figure 2c). Further increase in strain to $\varepsilon \approx 256$ results in a homogenization of the composite and a NC microstructure evolves, as seen in the transmission electron microscope (TEM) bright-field (BF) micrograph in Figure 3a. From high-resolution TEM images a grain size of 5–15 nm was determined.[63] In the Cu–47 at% Cr composite similar observations are made, the Cr particles are elongated and fractured, leading to a fine dispersion of Cr fragments in the Cu matrix. At an applied strain of $\varepsilon \approx 400$, a homogeneous NC structure is formed, with a somewhat larger grain size than in the Cu–51 at% W alloy of about 10–20 nm,[32] see TEM image in Figure 3b. The selected area diffraction (SAD) patterns displayed in Figure 3, reveal

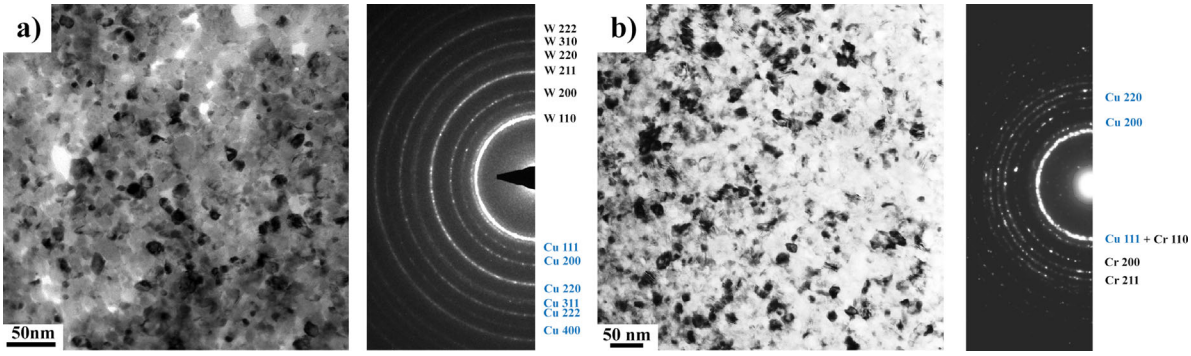

Fig. 3. TEM BF and corresponding SAD pattern in the saturation regime of deformation showing homogeneous NC microstructures. (a) The Cu-51 at% W composite at $\varepsilon \approx 256$ with a grain size of 5–15 nm. The SAD pattern reveals both Cu and W phases as labeled. b) Microstructure of the Cu-47 at% Cr composite at $\varepsilon \approx 400$ with a grain size of 10–20 nm, and SAD pattern with distinct diffraction rings of the Cu and the Cr phase (see labels).

ADVANCED ENGINEERING MATERIALS

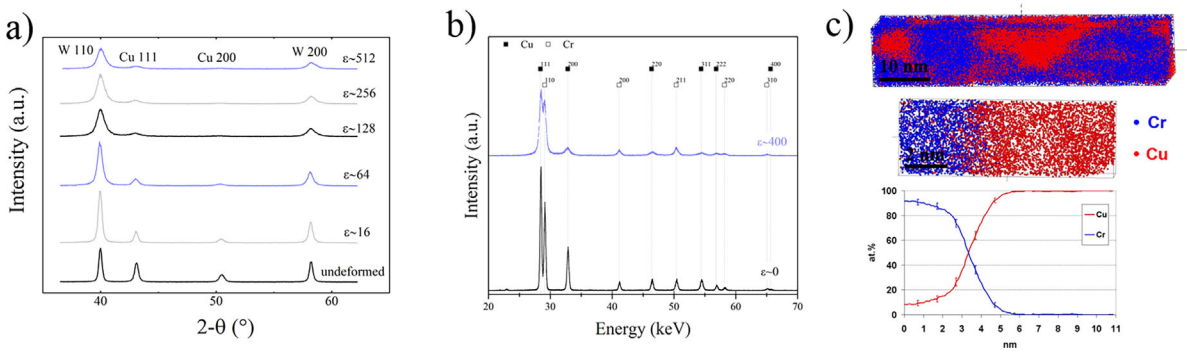

Fig. 4. (a) XRD patterns of the Cu-51 at% W composite recorded in the undeformed state and at different applied strains from $\varepsilon \approx 16$ to 512, revealing strong peak broadening due to grain refinement and peak shifts indicating dissolution of Cu and W. b) XRD pattern of the Cu-47 at% Cr for the undeformed state and at an applied strain of $\varepsilon \approx 400$, peak broadening, and shift is observed as well. c) APT analysis for Cu-47 at% Cr with reconstructed tip and local concentration profile revealing a dissolution of 15 at% Cu in the Cr phase and of 2 at% Cr in Cu.

that in both composites the initial constituent phases are still present (diffraction rings are labeled for Cu and W in Figure 3a and for Cu and Cr in Figure 3b).

Detailed diffraction analysis of larger volumes by X-Ray diffraction (XRD) measurements are displayed in Figure 4. XRD patterns of the Cu–51 at% W composite recorded in the undeformed state and at applied strain levels from $\varepsilon \approx 16$ to 512 reveal a strong broadening of the peaks due to the severe grain refinement. Additionally, the peaks are shifted from their position in the undeformed state, indicating lattice parameter changes and, hence, a dissolution of Cu in W and vice versa. Considering a "theoretical" fcc W lattice and using Vegard́s law, the solved amount can be roughly estimated. For this simple estimation, about 5 at% W is dissolved in the Cu phase and 4 at% Cu in the W phase, these values fit well to recent studies on sputter deposited Cu–W alloys.[64]

In the Cu-47 at% Cr composite, peak broadening and peak shift occurs in XRD measurements as well, indicating alloy formation (Figure 5b). Atom probe tomography (APT) offers information on the atomic scale distribution of the respective elements. An APT reconstruction from the as-deformed Cu-47 at% Cr composite is presented in Figure 4c showing Cu- and

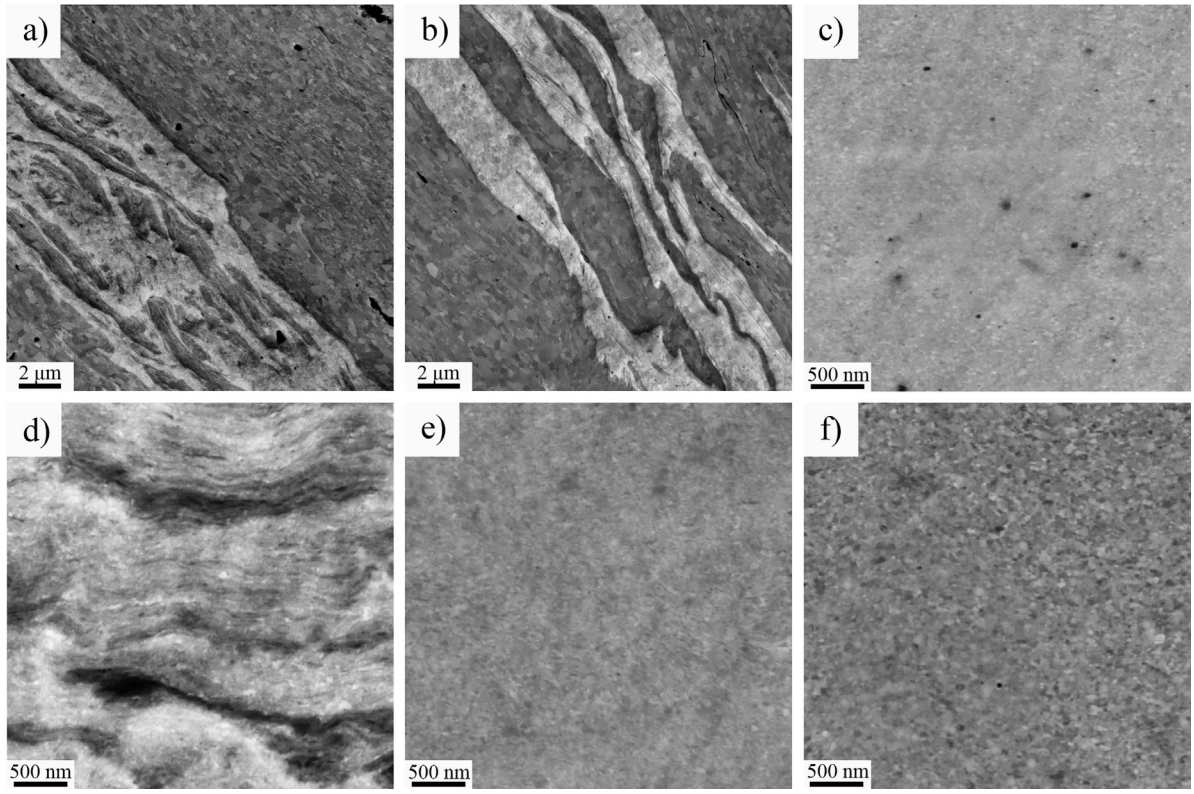

Fig. 5. BSE micrographs after the first HPT step at $\varepsilon \approx 40$ of (a) Cu-87 at% Fe and (b) Cu-73 at% Fe showing lamellar composites (Cu phase with bright and Fe phase with dark contrast) with UFG structures in the individual phases. BSE-SEM micrographs after the second HPT step (minimum $\varepsilon \approx 1\,100$), showing NC microstructures for (c) Cu-87 at% Fe, d) Cu-73 at% Fe, (e) Cu-53 at% Fe, and(f) Cu-17 at% Fe with chemical contrast only visible in the Cu-73 at% Fe (bright and dark bands indicating Cu-rich and Fe-rich regions).

Cr-rich grains separated by diffuse phase boundaries. A local concentration profile measured across a phase boundary reveals that the mixing occurs asymmetric. A considerable amount of about 15 at% of Cu is dissolved in the Cr phase, however, only 2 at% Cr could be solved in the Cu phase. In summary, the final microstructure obtained is a nanocomposite in Cu-51 at% W and Cu-47 at% Cr, with partial supersaturation of the constituent phases at very high applied strains.

Another investigated fcc-bcc system is Cu–Fe.[49] Four different compositions were deformed by the two-step HPT process, as described in the previous chapter. SEM images recorded at low applied strains after the first HPT step ($\varepsilon \approx 40$) reveal a different deformation behavior than in Cu–51 at % W and Cu-47 at% Cr. Both phases, Cu regions appear bright and Fe regions dark in this case, are elongated and a lamellar structure is formed for all four investigated compositions (exemplarily shown for Cu-87 at% Fe and Cu-73 at% Fe in Figure 5a and b). In the individual Cu and Fe phases, an UFG structure with grain sizes between 200 and 400 nm develops in the different composites.[49] Further, refinement of the composites is realized by continuous thinning of the Cu and Fe lamellae (co-deformation). After the second HPT step, all composites exhibit a NC microstructure (Figure 5c–f). Only in the Cu-73 at% Fe composite, bright and dark bands are still distinguishable, implying Cu and Fe-rich regions (Figure 5d). A homogeneous structure is seen for the other three compositions in SEM images (Figure 5c, e, and f). XRD measurements reveal that in the Cu-17 and 87 at% Fe composites the peaks of the minor phase, which are clearly visible after the first HPT step, are not observed after the second HPT step.[49] This indicates that single-phase supersaturated alloys are formed at high and low Fe content. In the medium composition range, Cu-53 at% Fe and Cu-73 at% Fe, a peak shift is observed after the second HPT step. However, Cu and Fe phases still contribute to the diffraction pattern and Fe–Cu composites composed of fcc Cu-rich and bcc Fe-rich solid solutions are obtained. APT analysis of the Cu-53 at% Fe composite reveals that a maximum of about 25 at% Cu is dissolved in the Fe phase, and about 20 at% Fe in the Cu phase.[49]

At the highest amount of applied strain, a NC microstructure is obtained in all three investigated fcc-bcc systems. Cu–W, Cu–Cr, and Cu–Fe form for medium compositions, where the phases exist in similar volume fractions, a nanocomposite with partial supersaturation of the respective phases. In the Cu–Cr and Cu–W systems, the deformation is governed by strong plasticity in the softer Cu phase, together with heavy elongation and repeated fracture of the harder W and Cr particles. In Cu–Fe, co-deformation of both phases occurs to a greater extent, which leads to complete single-phase supersaturated solid solutions for high and low Fe contents.

4.2. Fcc-Fcc

The fcc-fcc systems have been investigated by our group as well. Elemental powders were mixed in several compositions and processed by a single or two-step HPT process. In the Cu–Ag system, a lamellar structure is formed at low strains independent of composition as shown exemplarily for Cu-6 and 37 at% Ag in Figure 6a and d. In the individual Cu and Ag phases, an UFG structure is formed. The obtained saturation grain size is in the same range as observed also for the pure Cu and Ag powders deformed to saturation (see EBSD scans in ref.[54]). At higher applied strains, different deformation behaviors are observed in the composites, depending if the Cu and Ag phases are present in minor or balanced volume fractions. In the Cu-6 at% Ag composite, co-deformation and extensive refinement of both phases leads to a homogeneous NC microstructure (Figure 6b and c). In the Cu-37 at% Ag composite, extensive shear band formation (Figure 6e) prevents homogenization of the composite (Figure 6f).

As revealed by TEM investigations, the lamella thickness is reduced to several nanometer (Figure 7a) before shear band formation sets in in the Cu-37 at% Ag composite. Within the shear bands, a strong refinement to a nearly equi-axed NC structure is observed (Figure 7b and c). With increasing strain, new shear bands are formed continuously and a large part of the sample is transformed into this NC state (Figure 7d). The structure is characterized by a very high defect density, as seen from the strong contrast variations in TEM BF and dark-field (DF) images in Figure 7e, and from the significant broadening of the diffraction rings in the SAD pattern in Figure 7f. Diffraction rings of the Ag, the Cu and a supersaturated phase, which is generated in the shear bands, are present (labeled in Figure 7f). The occurrence of the formed supersaturated solid solution, which attains the global composition of Cu-37 at% Ag, is also confirmed by synchrotron XRD measurements.[65] In the Cu-37 at% Ag composite, the total imposed shear strain at very high strains is only carried by a limited number of shear bands (for details see ref.[65]). This prevents complete supersaturation and homogenization of the sample, instead a nanocomposite is obtained consisting of single-phase supersaturated regions (generated in the shear bands), and remaining lamellar dual-phase regions. Evaluation of peak shifts in the XRD measurements reveal that also in the lamellar matrix a partial supersaturation of the Cu and Ag phase (below 8%) occurs. In Cu-16 and 85 at% Ag composites, the maximum achievable degree of supersaturation is found to be about 23 at% Cu solved in Ag, while only 12 at% Ag could be solved in Cu. However, in the Cu-37 at% Ag composite, locally a supersaturated solid solution of 37 at% Ag in Cu can be attained inside the shear bands.

The second fcc-fcc combination, which has been investigated, are Ni–Ag composites. Ni-35 and 69 at% Ag composites were deformed in a single-step HPT process. As seen in Figure 8a, the Ni particles show almost no shape change after compaction of the powders, because the hardness is much higher than of the Ag powder. An applied strain of $\varepsilon \approx 90$ results in elongation and fracturing by necking of the elongated Ni particles (Figure 8b), which is similar as observed in the Cu-51 at% W and Cu-47 at% Cr composites

ADVANCED ENGINEERING MATERIALS

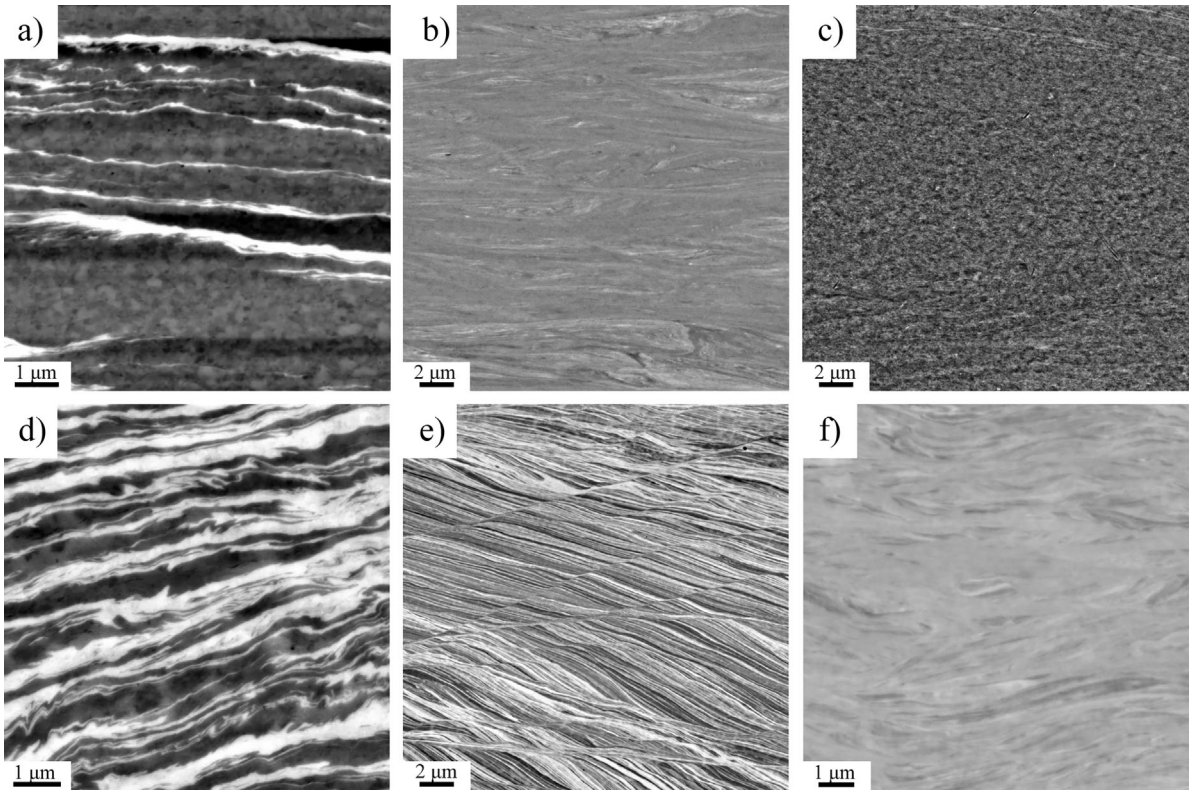

Fig. 6. BSE-SEM micrographs at different applied strains for the Cu-6 at% Ag composite (a) at $\varepsilon \approx 75$ showing a lamellar structure with thin Ag layers, (b) at $\varepsilon \approx 435$ revealing strong refinement of the composite, and (c) a homogeneous NC microstructure is obtained in saturation at $\varepsilon \approx 1\,100$. BSE-SEM micrographs of Cu-37 at% Ag (d) at $\varepsilon \approx 75$ showing a lamellar composite, (e) at $\varepsilon \approx 220$ revealing numerous shear bands, and (f) at $\varepsilon \approx 1\,100$ showing that inhomogeneities in the composite are still present.

(compare with Figure 2). Further deformation refines the composite to a lamellar structure (Figure 8c), as also observed in Cu–Fe and Cu–Ag composites. At higher applied strains, an inhomogeneous structure evolves due to strain localization in Ag-rich regions and pronounced shear band formation. UFG pure Ni regions are still retained besides strongly refined lamellar regions even at applied strains of $\varepsilon \approx 1\,800$ (see Figure 8d). Due to the higher Ag content, this inhomogeneous deformation is even more pronounced in the Ni-69 at% Ag composite (see Figure 8e and f).

Additionally, Ni–Ag composites, with a content of 6 and 19 at% Ag were deformed in a two-step HPT process. For these high Ni contents, co-deformation of both phases occurs also at higher strains. Similar as in the Cu–Fe composites, both phases are continuously refined. In the saturation regime, a NC microstructure is formed and full supersaturation was achieved (for details see ref.[60]).

4.3. Fcc-Hcp

As fcc-hcp model system, Cu–Co composites were chosen and three initial compositions, Cu-26, 54, and 76 at% Co, were investigated. The microstructure as a function of applied strain is presented in Figure 9 exemplarily for the Cu-76 at% Co composite. Similar observations are made in all compositions at low strains, the Co particles (dark contrast), which are slightly elongated as a result of the applied shear strain, are inhomogeneously distributed within the Cu (see Figure 9a). In the Cu-26 and 54 at% Co composites, the Co phase is embedded in the Cu matrix, while Cu is the minor phase in Cu-76 at% Co composite. By increasing the applied strain, further elongation and necking leads to refinement of the Co particles, see Figure 9b and c. It is proposed that the Cu matrix carries a large amount of the imposed strain, while the harder Co phase deforms mainly by necking and fracture of the particles, as also observed in Cu-51 at% W and Cu-47 at% Cr. In the individual Cu and Co phases, UFG structures are formed. Exceeding applied strains of about $\varepsilon \approx 100$ residual Co particles are still present in the Cu-26 and 54 at% Co composite. In the Cu-76 at% Co composite, a homogeneous microstructure is observed, although bands with bright and dark contrast indicate Cu- and Co-rich regions.[58] However, homogenous microstructures are reached, if only a small additional amount of strain is applied. The same is observed in the Cu-54 at% Co composite. In contrast, an applied strain of $\varepsilon \approx 500$ is needed for the Cu-26 at% Co composite to homogenize the microstructure on a microscopic level. Nevertheless, few Co particles are still visible in SEM micrographs. In all three compositions, NC microstructures are obtained at high applied strains, see Figure 10d–f for Cu-26, 54, and 76 at% Co, respectively. As can be seen from TEM diffraction patterns (Figure 9g–i), only fcc lattices are present for all compositions. A phase transformation of Co from hcp to fcc takes place during

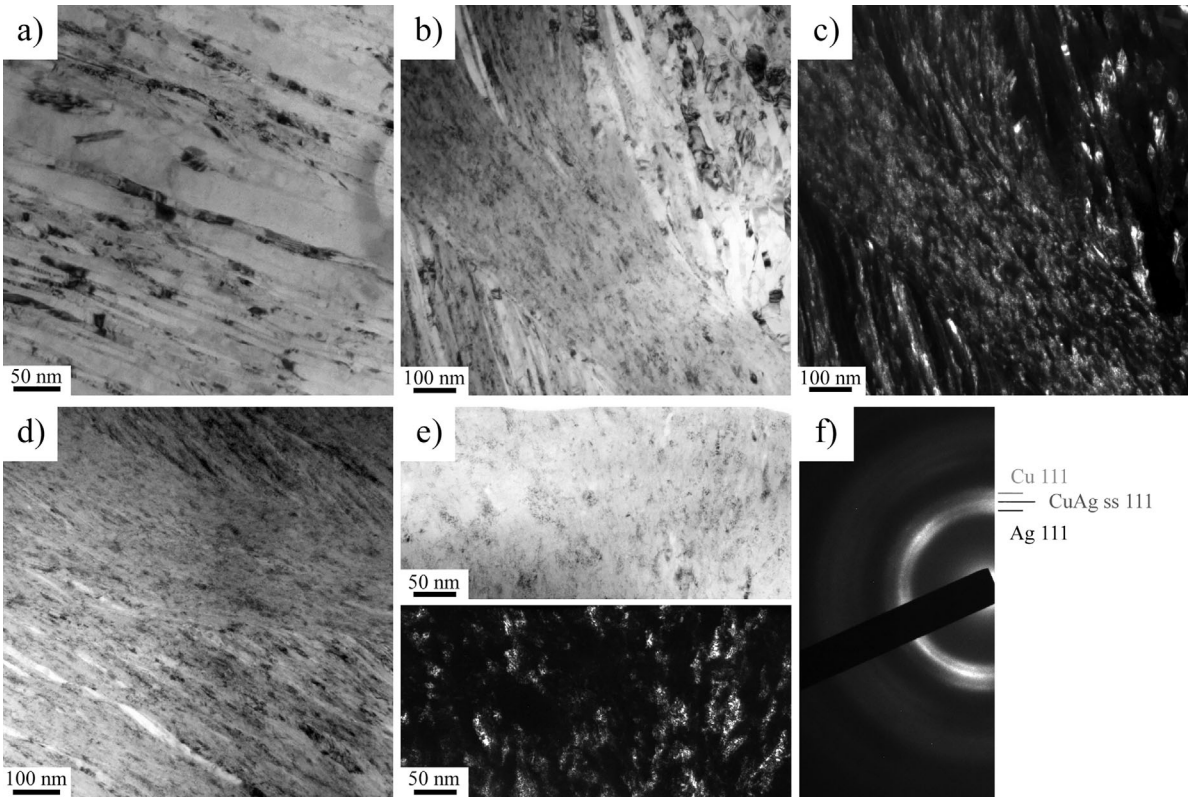

Fig. 7. TEM investigations on the Cu-37 at% Ag composite. (a) Nano-lamellar structure at $\varepsilon \approx 110$. (b and c) A shear band at $\varepsilon \approx 220$ in BF and DF mode revealing an equi-axed structure inside the shear bands. (d) A strong refinement by shear bands is observed at $\varepsilon \approx 1\,100$ with remaining lamellar regions. (e) BF and DF image at $\varepsilon \approx 2\,200$ revealing the very high defect density (see strong contrast changes in the images). (f) SAD pattern at $\varepsilon \approx 2\,200$, diffraction rings of Cu, Ag, and the supersaturated phase, which is formed in the shear bands, are indicated.

deformation,[66] which might be further promoted by the dissolved Cu.

To study the chemical intermixing on the atomic level, EELS (electron energy-loss spectroscopy) and APT analyses were conducted at different strain levels. A top view of an APT reconstruction for Cu-76 at% Co at a low applied strain of $\varepsilon \approx 30$ is shown in Figure 10a. The concentration profiles reveal different supersaturation levels in the Cu and Co phase (blue isoconcentration surface corresponding to 54 at% Cu). The concentration profile along cylinder A shows substantial dissolution of about 40 at% Co in the thin Cu region, but in the surrounding Co phase no Cu was detected. Also, no Co was dissolved in the larger Cu region on the left. Contrary, the concentration profile B gives a Cu concentration in Co up to 30 at% behind the thin Cu region. A reconstruction of an APT tip in a side and top view is presented in Figure 10b and c. The concentration profile (measured along the cylinder indicated in Figure 10c) reveals a Cu concentration of 30 at% in the thin Co phase, additionally, Co dissolved in the Cu phase as well with concentrations up to 40 at%. Thus, it can be concluded that the mixing process starts already at relatively low strains in the Cu-76 at% Co composite.

In the Cu-26 at% Co composite, Co particles persist even at the highest conducted strain level, as revealed by SEM and TEM.[57] Several EELS line measurements performed at a strain of $\varepsilon \approx 100$ across Co particles revealed an asymmetric mixing: A dissolution of up to 30 at% Co was observed in the Cu phase, while no Cu was detected in the Co grains. APT analyses at the highest applied strain level gives a local composition of 25.6 at% Co, which is in quite good agreement with the nominal composition of 26 at% Co. For the Cu-76at% Co composite, the average Cu concentration determined by APT is 22–24 at% in Co.[57] The concentration profiles obtained from EELS measurements from the Cu-54 at% Co composite at $\varepsilon \approx 440$, include several grains and show a relatively homogeneous distribution of Cu and Co (for details see ref.[58]).

In the saturation regime of deformation, a homogeneous distribution of Cu and Co atoms is observed as confirmed by APT analysis and EELS measurements in the Cu-Co composites (for details see refs.[57,58]). TEM diffraction data further indicates that a single-phase fcc solid solution has formed in composites with low and high Co content. Supersaturated solid solutions can be also obtained in the Cu-54 at% Co composite. However, due to the very similar lattice parameters of fcc Cu and fcc Co, it cannot be differentiated if the composite is completely single-phase or consists of a mixture of supersaturated Cu- and Co-rich grains with up to 45–50 at% Cu dissolved in Co and vice versa.

ADVANCED ENGINEERING MATERIALS

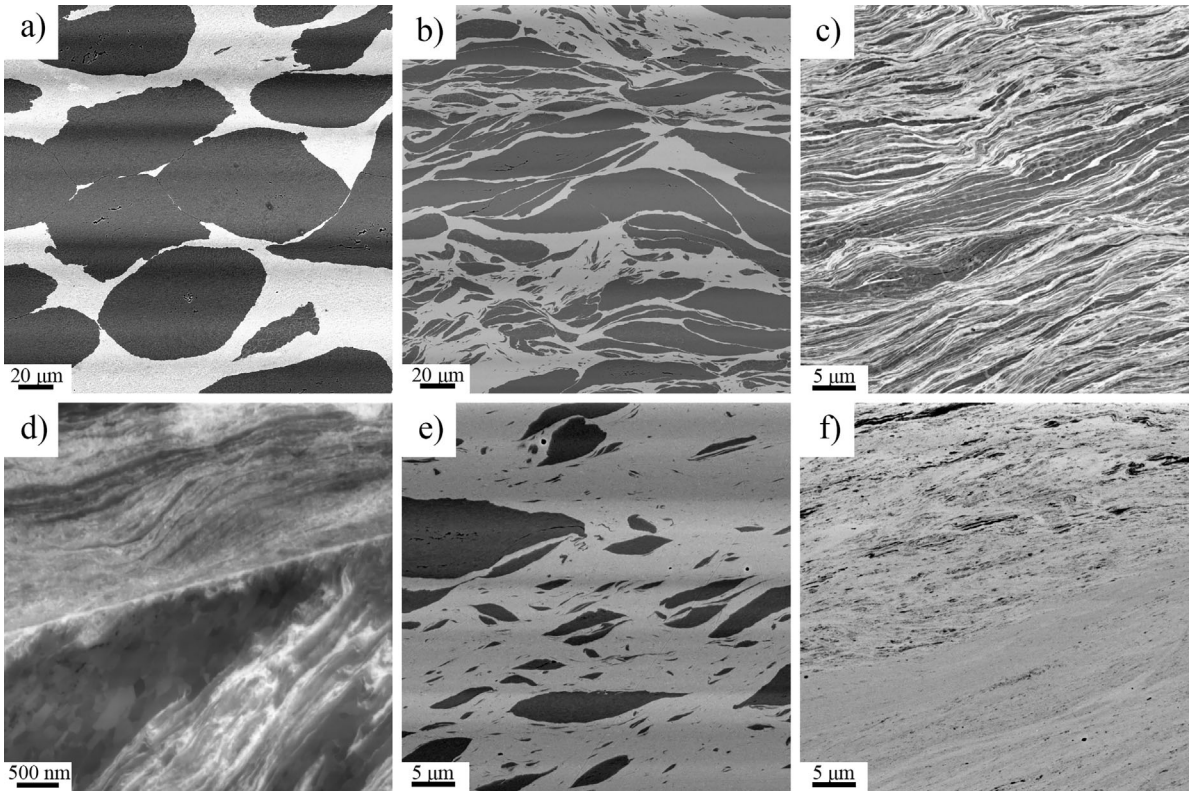

Fig. 8. BSE-SEM micrographs of Ni-35 at% Ag at (a) $\varepsilon \approx 0$ with Ni powder particles (dark contrast) embedded in Ag phase (bright contrast). (b) At $\varepsilon \approx 90$ showing elongation and fracturing of Ni particles. (c) At $\varepsilon \approx 180$ a lamellar structure has formed, and (d) at $\varepsilon \approx 1\,800$ inhomogeneities are still present. BSE-SEM micrographs of Ni-69 at% Ag (e) at $\varepsilon \approx 180$, where large Ni particles are still present, and (f) at $\varepsilon \approx 1\,800$ showing an inhomogeneous structure.

In summary, a deformation-induced supersaturation process during HPT deformation is observed in all studied composites. The maximum achieved solubilities for each investigated system are depicted in Figure 11 and summarized in Table 2. In the Cu-51 at% W and the Cu-47 at% Cr composites, the constituent phases are existent in similar volume fractions. Due to the high hardness of the W and Cr phase, the deformation process is characterized by strong local plasticity in the soft Cu phase and elongation and fracture of the harder W and Cr particles. Contrary, the Cu-53 at% Fe composite deforms by homogeneous thinning of both phases. Nevertheless, in all three composites, a partial supersaturation was obtained and the final NC microstructure is composed of Cu-rich grains and W/Cr/Fe-rich grains. In the Cu–Fe system, composites with high and low Fe content (17/87 at%) were successfully deformed to single-phase supersaturated solid solutions. In the two fcc-fcc systems, strong shear localization occurs in Cu-37 at% Ag and Ni-35 and 68 at% Ag, preventing a homogenization of the composites and, therefore, also only partial supersaturation is obtained. When the Ni content reaches high volume fractions (Ni-6 and 19 at% Ag), a more homogeneous deformation behavior is observed and single-phase supersaturated solid solutions are formed. The same is observed in Cu–Ag composites with high and low Ag content. The composites of the fcc-hcp Cu–Co system deform very similar to the Cu-51 at% W and Cu-47 at% Cr composites. The softer Cu phase carries a large amount of the applied strain, while Co is refined mainly by elongation, necking, and fracturing. However, although local chemical analyses exhibit high levels of supersaturation, the very similar lattice constants of fcc Cu and fcc Co prevent a clear differentiation between Cu-rich and Co-rich phases in diffraction experiments for medium compositions.

In single-phase pure metals or alloys, the achievable minimum grain size in saturation is usually in the UFG regime and is mainly governed by the material (e.g., alloying significantly reduces the saturation grain size) and the processing parameters (i.e., deformation temperature, strain, strain path). In immiscible composites, much smaller grain sizes of 100 nm and less are observed as summarized in Table 1.

Two different cases can be distinguished: In the composites, in which full supersaturation was obtained, the grain size at RT is controlled as in single-phase pure metals and conventional alloys by the grain boundary mobility and the amount of alloying elements. With increasing alloying content, the grain boundary mobility and, thus, the saturation grain size is reduced (see, e.g., Cu–Ag and Cu–Co in Table 1).

Before full supersaturation is attained, the phase dimensions first reach sizes below the saturation grain size until the dissolution of these nano-sized particles accomplishes continuously, and a larger saturation grain size is stabilized in the homogeneous single-phase alloy, as for example,

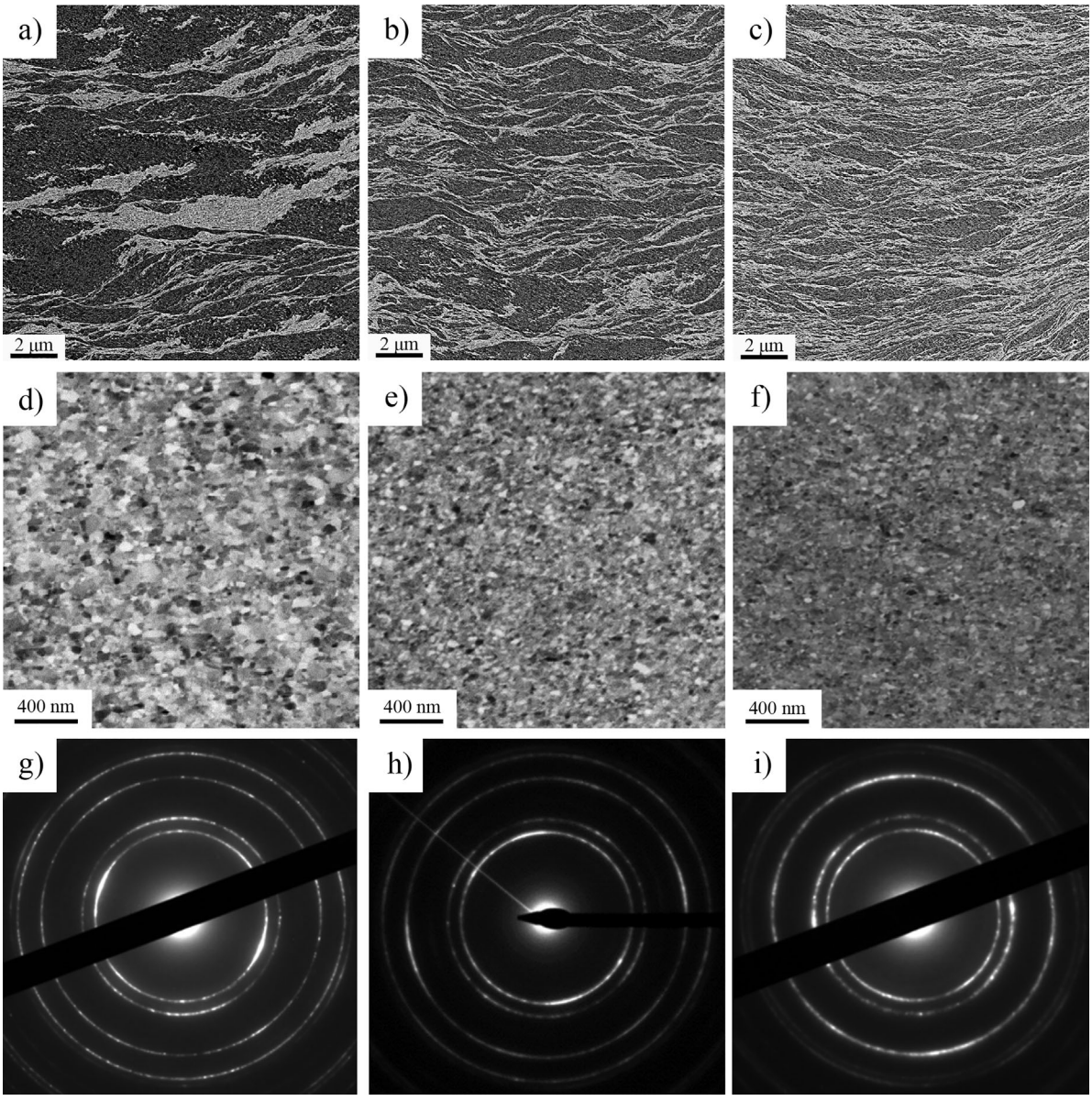

Fig. 9. BSE-SEM micrographs of the Cu-76 at% Co composite at (a) $\varepsilon \approx 10$, (b) $\varepsilon \approx 25$, (c) $\varepsilon \approx 100$ showing elongation and fracturing of the Co phase. BSE-SEM micrographs of the microstructures at the highest amount of applied strain for (d) Cu-26 at% Co, (e) Cu-54 at% Co, and (f) Cu-76 at% Co with corresponding diffractions patterns for (g) Cu-26 at% Co, (h) Cu-54 at% Co, and (i) Cu-76 at% Co revealing NC fcc structures.

observed in Cu-Co. In partially supersaturated composites with dual-phase structures after HPT deformation even smaller grain sizes of about 10–20 nm are observed (see Cu–W and Cu–Cr in Table 1). The physical deformation mechanisms of these nanocomposites in the saturation regime are still not clear and further research is definitely needed.

5. Process of Deformation-Induced Mixing

The mechanism behind deformation-induced supersaturation, although intensively investigated, is still under debate.[33,39,69] The proposed concepts and their relevance to our studies will be summarized in the following section.

To explain the observed intermixing during ball milling experiments, Bellon and Averback proposed a mechanical mixing mechanism, the so-called "kinetic roughening model."[42] In Monte Carlo simulations, they showed a roughening of phase boundaries through extensive dislocation activity across these boundaries in fcc-fcc systems. In later studies, they investigated also bcc-fcc phase boundaries by MD simulations, where dislocation transfer is in principal constricted.[70] The simulations showed no roughening of interfaces, however, mixing still occurred, and the authors explained this by dislocation pile-up at the boundaries. This leads to disordered regions, where the energy barriers are lowered, and local mechanical instabilities result in atom exchanges. They also studied the influence of different kind of

ADVANCED ENGINEERING MATERIALS

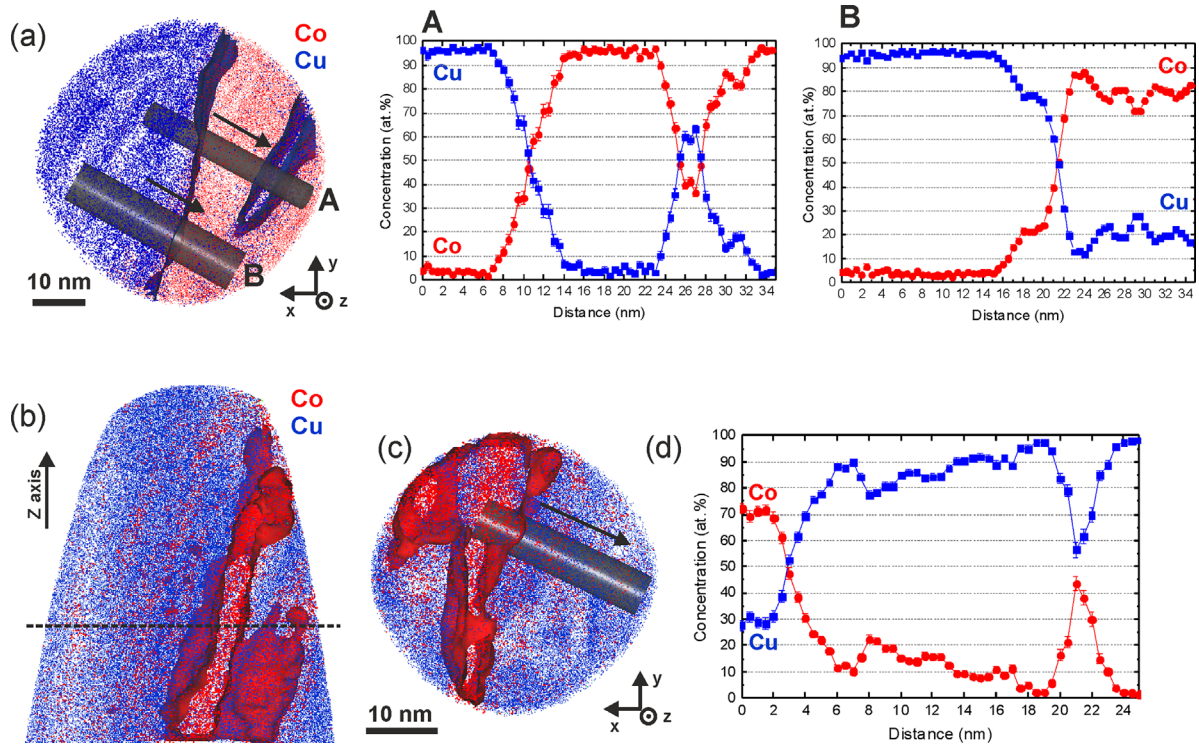

Fig. 10. APT reconstructions of a Cu phase in Cu-76 at% Co ($\varepsilon \approx 30$): (a) Tomographic slice (top-view, thickness of 10 nm), in which the blue isoconcentration surface corresponds to 54 at% Cu. 1D-concentration profiles are computed along the region-of-interests ("A" and "B"), (b) tomographic slice (side-view, thickness of 10 nm), in which the red isodensity surface corresponds to 14 Co atoms nm^{-3}, (c) top-view of a tomographic slice along the z-axis as marked in (b) by dotted line with a thickness of 10 nm, and (d) 1D-concentration profile plotted along the marked region-of-interest in (c). Reproduced with permission from ref.[52] Creative Commons Attribution License (CC BY 4.0) 2016 Elsevier.

interfaces on the mixing process. In general, in processes, which implicate a transport of atoms across interfaces by dislocation glide, the phase boundaries have to fulfill certain criteria. Embury et al.[71] defined the following points: The resolved shear stress at the boundary resulting from dislocation pile-up should be a maximum on the activated system, the misorientation of the active slip planes in the two involved grains should be a minimum, and the configuration of the boundary should be one of minimum energy. It is evident, that these criteria are easier fulfilled in fcc-fcc systems, however, in fcc-bcc these conditions apply, if a Kurdjumov-Sachs orientation relationship is present, which was indeed observed in Cu–Nb sheets produced by ARB.[72] Misra and Hoagland[73] showed that in ARB Cu–Nb, the shear stress on dislocation is high enough to cross interfaces when layer thicknesses below 5 nm are reached. Orientation relationships between the constituent phases resulting from a shear texture, which is often observed in HPT processed materials,[45] is seen, for example, in Cu–Ag composites. An orientation relationship between Cu and Ag could facilitate a mixing process by dislocation glide across phase boundaries. In addition, the phase spacing is in the nanometer range, see Figure 7, which is necessary to reach stress levels for interface cutting according to the study by Misra and Hoagland.[73] As revealed by XRD synchrotron measurements, massive mechanical mixing occurred in the shear bands, but also in lamellar regions, a partial supersaturation of Cu and Ag was observed. While the deformation mechanism in the shear bands is still unclear, it is assumed that the lamellar matrix deforms by dislocation plasticity, which gives indication for a mechanical mixing by dislocations crossing interfaces. In the Cu–Co composites, in which fcc-hcp phase boundaries are present, a lattice change in the Co phase from hcp to fcc could enable such a mixing process. In the saturation regime of deformation, the "kinetic roughening model" predicts that the degree of intermixing is determined by an equilibrium between mechanical mixing at interfaces and decomposition by thermal diffusion. Thus, by increasing the deformation

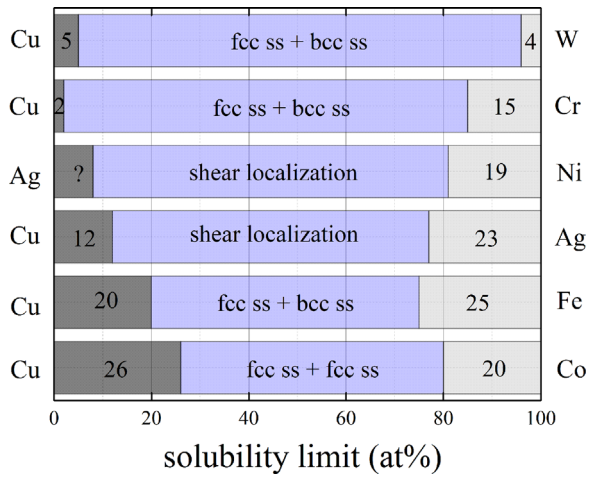

Fig. 11. Maximum achieved solubility in the different investigated systems.

Table 2. Summary of mixing enthalpies taken from literature, atomic radius mismatch (ratio of the atom species with smaller r_{small} and larger r_{large} atomic radius) and maximum obtained solubility from our experiments of the constituent phases in each investigated system.

	Cu–Ag	Cu–Co	Cu–Fe	Cu–Cr	Ni–Ag	Cu–W
ΔH_{mix}	6 kJ mol^{-1}[67]	6.3 kJ mol^{-1}[3]	12 kJ mol^{-1}[9,68]	20 kJ mol^{-1}[57]	15 kJ mol^{-1}[38] 23 kJ mol^{-1}[67]	35.5 kJ mol^{-1}[2]
r_{small}/r_{large}	12%	2.5%	1.5%	0%	14%	8%
Max solubility	≈12 at% Ag in Cu ≈23 at% Cu in Ag	≈22–24 at% Cu in Co ~40–50 at% Co in Cu (medium) ≈26 at% Co in Cu	≈20 at% Fe in Cu ≈25 at% Cu in Fe	≈2 at% Cr in Cu ≈15 at% Cu in Cr	≈19 at% Ag in Ni	≈5 at% W in Cu ≈4 at% Cu in W

temperature, the degree of supersaturation is lowered, this is indeed observed, for example, in Cu–Ag.[53]

Raabe et al. considered as well dislocation motion across phase boundaries in their so-called "dislocation shuffling" model.[39] They assumed that multiple dislocation glide events on several planes across interfaces will move small particles into the other phase, and after repeated dislocation cutting processes, they will eventually dissolve due to the Gibbs–Thomson effect. They also indicated that the mixing process could be assisted by shear banding. A similar approach was contemplated by Yavari et al.[8] for mechanical mixing during ball milling. They assumed that small tips of one phase with a radius of only 2 nm or less are formed, and the atoms on the tip will dissolve due to capillary pressure (Gibbs–Thomson effect). Such small fragments of Fe in a Cu–Fe composite were indeed observed by Sauvage et al.[30]

Other studies take the modification of phase or grain boundaries during SPD processing into account, for example, Veltl et al.,[74] who suggested that the energy stored in the boundaries facilitates the intermixing. So-called "non-equilibrium" grain boundaries, as proposed by Valiev,[75] are suggested to have increased capability to promote diffusion and also influence on the mechanical properties. As assumed by Sauvage et al.,[33] such a modification of interfaces is necessary to enable dislocation glide across phase boundaries and subsequently to transfer atoms into the other phase.[33] Additionally, very high vacancy concentrations during HPT deformation, together with the special configuration of grain or phase boundaries could enable defect-enhanced diffusion processes.[10,76] However, due to the positive mixing enthalpy, there is in principal no thermodynamic driving force for mixing by diffusion.

In HPT processing, the very high applied strains, which are obviously needed to induce chemical mixing, must be taken into account. In studies on Al alloys with Al_2O_3 particles, it was shown that it takes enormous strains to homogeneously distribute the particles, which agglomerate in clusters.[77] A process similar to erosion was proposed. In systems with a hard minor phase, for example, Ni–Ag with low Ni content, such an erosion process could also take place on the atomic scale. Another mechanism, which takes the large amount of applied strain into account, is a fracture and rebonding process.[59] In Cu–W and Cu–Cr, it appeared that the harder particles fracture repeatedly, and the softer phase fills the gap in between the broken particles. This Cu in between is deformed under high pressure, and could eventually dissolve in the other phase. These processes are independent of structural sizes and would start immediately with deformation. In the Cu–Co composites, it was indeed shown, that the mixing process starts at relatively low strains ($\varepsilon \approx 30$ in the Cu-76 at% Co composite).[58] In APT analyses on Cu–Co, an increased solute content was observed near nanometer sized particles, but no distinct chemical gradients were observed at interfaces, see Figure 10. The lack of intermixing at phase boundaries and the increased solute content behind small particles at low applied strains in Cu–Co can be attributed to a process similar to abrasion, instead of a mixing based on dislocation motion across phase boundaries. However, it is assumed that the final dissolution at high applied strains could be realized by a dislocation-shuffling mechanism or defect-enhanced diffusion.[58]

The first group of proposed mixing mechanisms coincide in one point, that the supersaturation process is controlled by the strain level, hence, a critical phase dimension in the nanometer regime is needed to induce the mixing process. The following criteria, established in the different approaches, are fulfilled, if this phase dimensions are reached:

1) Stresses on dislocations are high enough to enable dislocation glide across phase boundaries.
2) Possible phase transformations can occur, as for example, in Co from hcp to fcc.
3) A huge amount of interfaces is available, which on the one hand show special characteristics in SPD processed materials, and on the other hand offer many sites for the mixing process.
4) Particles reach sizes below a critical level for dissolution by the Gibbs–Thomson effect.

Additionally, shear banding can provide high amounts of strains, accelerating the local mixing process.

The second group of mixing mechanisms accounts for the large amounts of strain applied during HPT processing. Mechanisms with similarities to erosion or abrasion were proposed. In this case, the supersaturation process would start immediately with the deformation process, but it would

require very high amounts of applied strain to homogenize the composites. These processes are mainly contemplated for composites with a hard second phase, like Cu–W, Cu–Cr, and Cu–Co. Similar assumptions are true for defect-enhanced diffusion processes, if a high defect concentration level is reached, mixing should start independently of structural sizes.

6. Influencing Factors

6.1. Lattice Structures

As proposed in several studies, dislocation glide across phase boundaries accounts for the dissolution of the constituent phases and, therefore, the lattice structures could have an influence on the solubility limit. As seen in Figure 11, the system with the highest achieved solubility are the fcc-hcp Cu–Co, in which supersaturated solid solutions with local concentrations of up to 50 at% Cu and Co were obtained. In Cu–Co composites, the fragmentation process generates Cu and Co particles having nanometer dimensions. APT and EELS analysis revealed that mixing starts already at relatively low applied strains in those nanometer phases. Moreover, it was shown that a lattice change in Co from hcp to fcc occurred at grain sizes below 100 nm,[66] this could facilitate further mixing of Cu and Co at high strains. The developed supersaturated solid solutions exhibit, therefore, a fcc lattice at all compositions. Although in Fe a phase transformation to fcc is possible at grain sizes below 5 nm,[78] no indications for such a lattice change was provided in our studies. In the Cu–Fe system, the fcc phase is stabilized in composites with up to 20% Fe, while the bcc phase is stable up to 25% Cu in Fe. In the intermediate composition range, a mixture of fcc Cu-rich and bcc Fe-rich phases is obtained. The same is observed in the other fcc-bcc systems, Cu–W and Cu–Cr, in which the Cu–W system is the one with the lowest solubility. Only 5 at% W could be dissolved in Cu and 4 at% Cu in W. Based on the results for the different immiscible systems, different lattice structures are not a barrier for the supersaturation process.

6.2. Hardness Differences

In contrast to single-phase materials, a complex hardening behavior is usually observed in composites. The hardness as a function of applied strain is shown in Figure 12 for Cu-54 at% Co, Cu-37 at% Ag, and Cu-47 at% Cr. Such hardness profiles, with three distinguishable stages are characteristic for binary immiscible composites. In the beginning of the deformation process of the composites, the present phases have dimensions in the micrometer regime, see for example, bulk materials (Cu–W in Figure 2), or powders (Ni–Ag in Figure 8), which are usually between 10 and 50 μm. In the very beginning, a steep hardness increase from the hardness level of the undeformed material to the first plateau is observed in the hardness evolution, as indicated in the schematic hardness plot in Figure 13. This hardness increase is induced by the deformation due to the compression to build up the applied pressure and the subsequent shear deformation, which causes the formation of substructures in the individual phases. However, this first increase is experimentally not captured in the hardness measurements, because it usually begins to saturate at $\varepsilon \approx 1$. In the hardness evolution of the Cu-47 at% Cr composite in Figure 12c, the hardness level of the undeformed material is also included, before $\varepsilon \approx 1$ is reached the hardness already increases from ≈100 to ≈200 HV. At low applied strains, a constant hardness level or a slight increase is observed (continuous and dashed line labeled as stage A in Figure 13). In stage B, the hardness strongly increases due to extensive refinement of the microstructure. Different deformation mechanisms are responsible in different material systems, which depends on kind and volume fraction of the present phases, as discussed in detail in the following. After stage B, a saturation regime is reached (stage C), where the hardness is at a constant level, although a minor increase or decrease could be observed in some cases due to solid solution hardening or softening (indicated by dashed lines).

Figure 13 displays, schematically, the influence of the hardness differences and volume fraction of the phases on the microstructural evolution and deformation. One important point for co-deformation is the hardness difference (or the yield strength difference) of the respective components of the composites under HPT conditions. In case of large hardness differences between the phases, they will generally not deform to the same extent. If the hard phase has a minor volume fraction, this is even more pronounced. From our microstructural observations of the Cu–W, Cu–Cr, Cu–Co, and Ni–Ag composites, it is clearly visible that plastic

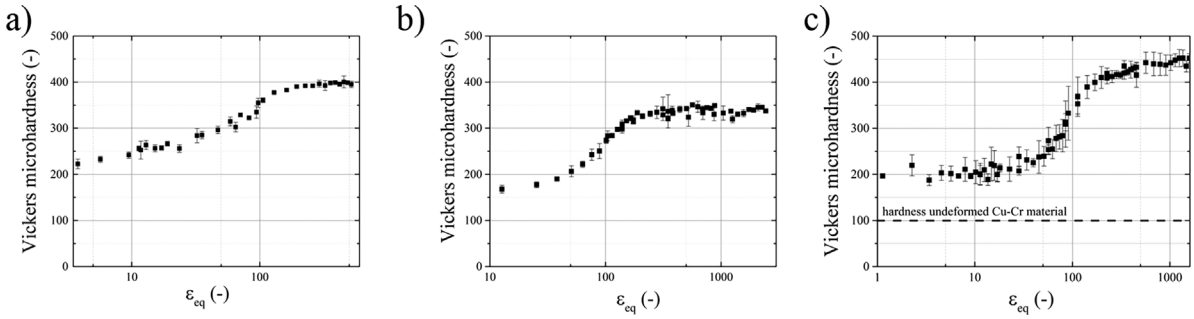

Fig. 12. Vickers microhardness as a function of applied strain for (a) Cu-54 at% Co, (b) Cu-37 at% Ag, and (c) Cu-47 at% Cr. Please note the logarithmic scale for the shear strain.

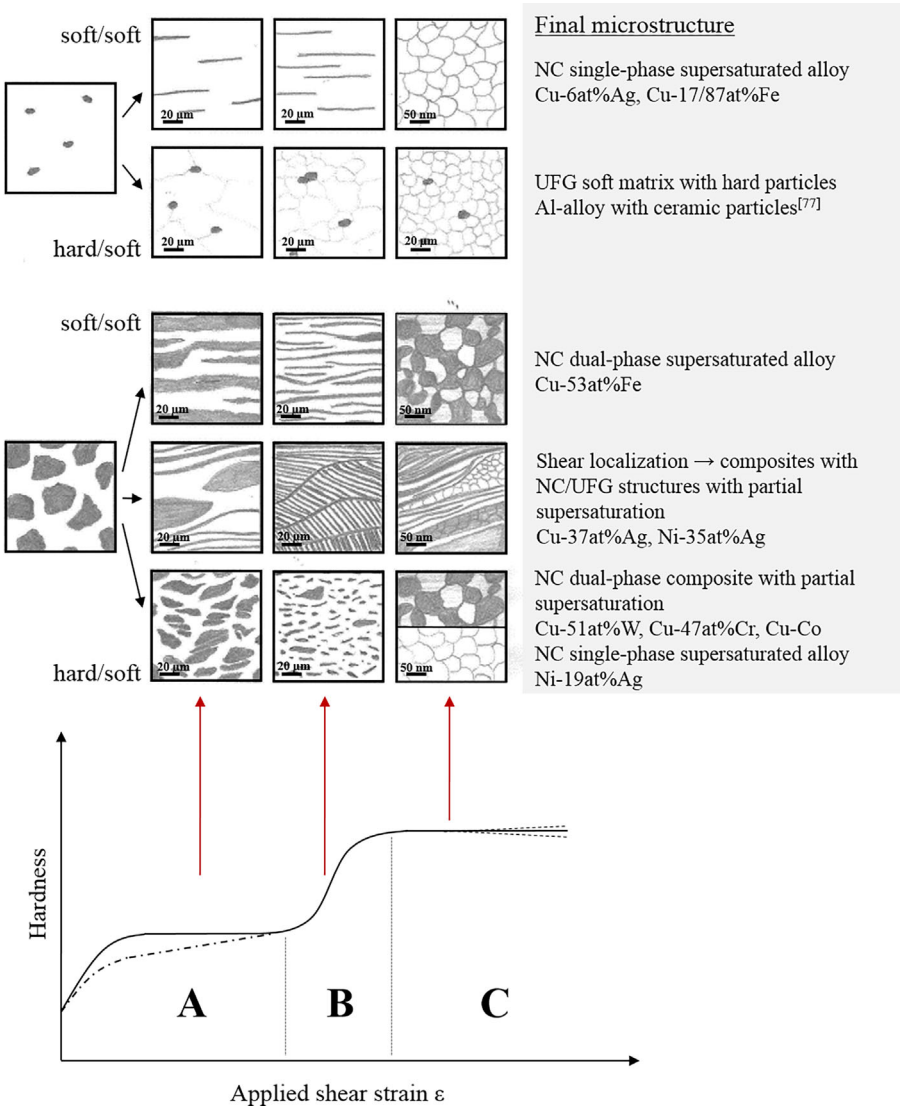

Fig. 13. Schematic of the microstructural and hardness evolution as a function of applied strain depending on hardness differences and volume fraction of the constituent phases. Please note the hardness evolution is sketched in a logarithmic scale for the shear strain.

deformation is mainly localized in the soft matrixes. As a consequence, the soft phase will carry most of the deformation. In the beginning of the deformation process, the softer matrix will form an UFG saturation structure, with a lower hardness level than the hard phase, corresponding to the first stage A in the schematic hardness evolution. Although the hard phase show some deformability, fracturing predominates over plastic deformation. Due to the lack of co-deformation, it might be assumed that the local strain in the soft phase is also larger.[58] Plastic instabilities might further support the refinement process of the hard particles. On the mesoscopic scale, the instabilities can be caused by the aforementioned strain localization. On the other hand, microscopic plastic instabilities as described, for example, in refs.[79–81] might also occur. These instabilities are important on a smaller length scale, especially for very fine, nanometer-sized phases, as for example, experimentally observed in Cu–Co composites (Figure 10).

If the volume fraction is low enough, the hard particles will flow in the soft matrix, see schematic in Figure 13, and only in rare cases, two particles could get bonded and fractured again. This was experimentally observed in Al alloys with ceramic particles (SiC and Al_2O_3),[77] in which an extreme hardness difference between the phases is present. This could be also the case, for example, in a Cu–W composite with a very low volume fraction of W. If the volume fraction of the hard phase is low enough that contact between particles is limited, the hardness evolution would reflect only the hardening behavior of the soft matrix, in this case, no stage B and C are observed.

The deformation behavior is dependent on the volume fraction of the hard phase, as observed in the Ni–Ag and the Cu–Co system. Comparing the microstructures of Ni-35 at% Ag and Ni-69 at% Ag at the same applied strain (see Figure 8c and e) reveals that the refinement process of the Ni particles is much slower in the Ag-rich sample. However, the volume fraction of Ni in both cases is too high, that they could

flow unhindered in the Ag matrix. Therefore, a refinement of the Ni particles takes place, which again leads to a strong hardness increase (stage B in the schematic hardness plot) before a constant hardness level is reached (saturation regime C). However, even at very high strains, small Ni particles are retained and localized deformation mechanisms like shear banding lead to inhomogeneous microstructures. Similar observations are made in the Cu–Co system. The Cu-26 at% Co composite requires higher applied strains than the Cu-54 and 76 at% Co composites to homogenize, and even at the highest applied strain level Co particles are retained. Nevertheless, mixing occurs in the Cu-26 at% Co composite and a homogeneous alloy could be obtained, if the strain is further increased. In contrast, if the minor phase has a similar hardness than the matrix, both phases will co-deform, as for example, in Cu-6 at% Ag (see Figure 6) and Cu-17 and 87 at% Fe, see schematic in Figure 13. In the individual phases, the respective UFG saturation microstructures are formed in the beginning (regime A in the hardness plot). The minor phase is continuously thinned until it will dissolve (stage B) and a single-phase NC microstructure is formed (stage C).

When the hard phase has a large volume fraction, as for example, in Cu-51 at% W (see Figure 2), Cu-47 at% Cr, Ni-6 and 19 at% Ag, and Cu-54 and 76 at% Co (see Figure 10), both phases have to deform, although it is assumed that the soft phase will carry more deformation. The harder phase (W, Cr, Ni, and Co) is refined continuously by elongation, repeated fractures or necking and fracture. The soft phase (Cu and Ag) forms its respective UFG saturation microstructure in the very beginning of the HPT process, and then plastically deforms by dislocation motion and restores the microstructure by grain boundary motion.[44] During continuing deformation, both phases are further thinned, the hardness evolution in some cases shows first a slight hardness increase, see for example, Cu-54 at% Co (hardness plot in Figure 12), as long as the hard phase is still in micrometer regime. Then a strong hardness increase is observed (regime B), when both phases undergo severe refinement. In Cu-51 at% W and Cu-47 at% Cr, no full mixing was observed and the final NC microstructure obtained in regime C is composed of supersaturated Cu and Cr/W phase. In Ni-19 at% Ag, the Ni volume fraction is high enough, that all of the soft phase is dissolved in the hard phase (compared to Ni-35 and 69 at% Ag). Hence, the final structure is a NC single-phase supersaturated solid solution.

In the Cu-37 at% Ag and the Cu-53 at% Fe composites, the constituent phases have similar volume fractions and the hardness difference is not very pronounced. In the beginning of the HPT process (regime A), both phases reach their respective saturation grain size and hardness. In the Cu–Fe system, although co-deformation takes place, no supersaturated single-phase alloy is obtained in the medium composition range, instead a composite with partially supersaturated fcc Cu and bcc Fe is obtained, as in Cu-51 at% W and Cu-47 at% Cr. The Cu-37 at% Ag composite behaves differently, see schematic in Figure 13. In the beginning (regime A), both phases arrange in a lamellar structure with UFG structures inside the lamellae as in Cu–Fe composites. When a critical strain is reached, strong shear localization occurred, which was also observed in the Ni-35 at% Ag composite. In the Cu-37 at% Ag composite, a supersaturated phase was generated inside the shear bands, which had the global composition of the composite. The steady formation of new shear bands and connected lamella rotation (see Figure 6e), results in an accelerated refinement of the composite accompanied by a strong hardening (stage B). Because the shear bands cut through the lamellar regions under certain angles, the deformation is similar as in a two-step HPT process. In the saturation regime C, the deformation is mainly carried by shear bands, preventing full supersaturation of the composites and dual-phase lamellar regions are retained even at the highest applied strains. In the Ni-35 at% Ag composite, pronounced inhomogeneities in the microstructure are observed as well, see Figure 8d, reaching from pure Ni and Ag regions with UFG structures to nanocomposite regions with partial supersaturation.

In all composites, a strong hardness increase is observed due to a refinement to a NC microstructure, as summarized in Table 1. The deformation mechanisms, which maintain the microstructure in the saturation regime are not clearly identified. In the case of single-phase supersaturated solid solutions, as for example, in Ni-6 and 19 at% Ag, Cu-6 at% Ag, and Cu-17 and 87 at% Fe, it can be assumed that the same mechanisms operate as in pure metals or other single-phase alloys.[44] In the alloys with medium compositions in the fcc-fcc systems (Cu–Ag and Ni–Ag), only few shear bands carry most of the imposed strain. When a partially supersaturated composite is formed (as e.g., in Cu–W, Cu–Cr, and Cu–Fe), a possible mechanism is an equilibrium state between dissolution of atoms by deformation and decomposition by thermal diffusion. However, the deformation processes to realize the high shear strains are not yet understood.

6.3. Heat of Mixing

Table 2 lists the heat of mixing data available in literature and the atomic radius mismatch for each system. The system with the largest positive heat of mixing, Cu–W (ΔH_{mix} of 35 kJ mol^{-1}) has indeed the lowest solubility limit. Also the Ni–Ag and Cu–Cr systems, follow this trend with ΔH_{mix} of 23 and 20 kJ mol^{-1}, respectively, they have maximum solubilities of less than 20 at%. Interestingly, the Cu–Ag system, which has the lowest heat of mixing of all studied systems, does not show a higher solubility limit. It is even lower than in Cu–Fe or Cu–Co system. As shown in the previous section, strong strain localization in shear bands leads to the formation of a supersaturated solid solution with 37 at% Ag dissolved in Cu, which corresponds to the global composition of the alloy, but the absent deformation of the remaining lamellar matrix results in a retardation of supersaturation process. The Cu-based fcc-bcc composites could give evidence, if the heat of mixing or hardness

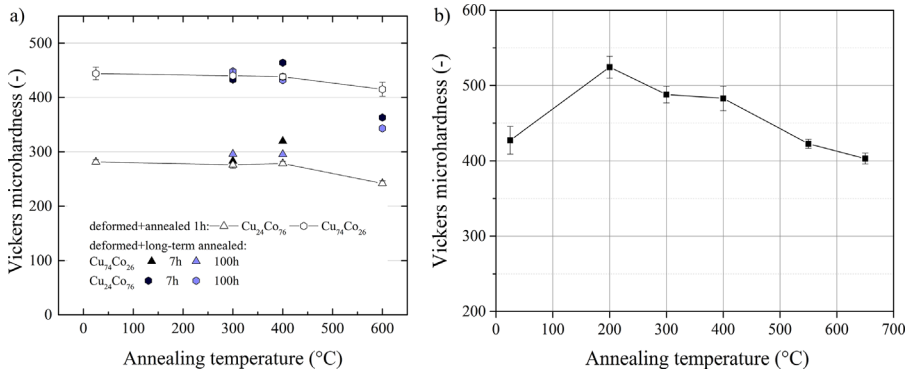

Fig. 14. Hardness as a function of annealing temperature: (a) for the Cu-47 at% Cr composite annealed at different temperatures for 30 min and (b) for the Cu-26 and 76 at% Co composites annealed up to 600 °C for annealing times of 1–100 h.

differences of the present phases governs the mixing process, however, the level of the heat of mixing correlates with the hardness difference (Cu–W has the highest heat of mixing and hardness difference, followed by Cu–Cr and Cu–Fe). Therefore, it cannot be concluded, which factor defines the maximum achievable solubility. However, in particular the Cu–Ag system demonstrates that a low positive heat of mixing is no indicator for a successful supersaturation to a single-phase alloy during HPT processing. It seems that the deformation behavior influences the maximum achievable degree of supersaturation in the Cu–Ag system by limiting homogeneous deformation of the composites.

7. Remarks on Thermal Stability

In general, the metastable supersaturated phases are expected to undergo phase separation upon annealing, which is indeed observed above certain annealing temperatures. In the Cu–47 at% Cr composite, the deformed microstructure is composed of nanometer sized grains (10–20 nm) with partial supersaturation (≈15 at% Cu is dissolved in the Cr phase and ≈2 at% Cr in Cu phase). During annealing at 400 °C, complete phase decomposition occurs and a nanocomposite with pure Cu and Cr grains evolves, in which grains of the same phase are isolated by grains of the other phase (for details see ref.[59]). The hardness after annealing for 30 min is stable up to 600 °C, at annealing temperatures between 200 and 400 °C even a hardness increase is observed (Figure 14a). In immiscible systems, this phenomenon is a common feature (also documented in Cu–Fe,[49] Cu–Ag,[53] and Cu–Co[56]), however, the details of this hardening during annealing are still unclear.

The supersaturated Cu-26 and 76 at% Co alloys were annealed for 1 h in air at 300, 400, and 600 °C, corresponding to ≈35, ≈40 and ≈52% of the melting temperature and additionally, to study the long-term stability, for 7 and 100 h, see Figure 14b. At the lowest annealing temperature of 300 °C, no significant change in hardness was observed independent of annealing time. A drop in hardness is not observed until the highest annealing temperature of 600 °C is reached. In the Co-rich composite, the hardness drops after 7 h annealing treatments, and after 100 h, a further slight decrease is observed. In the Cu-26 at% Co composite, the hardness decreases after 7 h annealing and then keeps a constant level. The thermal stability and decomposition behavior was studied in detail for the Cu-26 at% Co composite.[56] The grain size of this composite is about ≈100 nm. During annealing at medium temperatures (400 °C), a process similar to spinodal decomposition presumably takes place. This is indicated by chemical modulations inside the grains in form of an array of alternating Cu and Co, which was analyzed by EELS and APT, for details see ref.[56] This type of decomposition is observed inside the grains, because diffusion distances are very limited at 400 °C and beneath and the grain size is relatively large (compared to the other investigated systems, which all exhibit grain sizes well below 50 nm. The formed structures of phase-separated Cu and Co regions in the nanometer regime, together with Cu and Co particles, which formed at grain boundaries, show an extraordinary high long-term stability. In summary, the nanocomposites formed after annealing exhibit a high resistance to grain growth.

8. Summary and Conclusions

In summary, the investigated material systems can be divided into three groups with respect to their deformation behavior. First, the composites exhibiting strong hardness differences of the constituent phases, which are the Cu–W, Cu–Cr, Cu–Co, and the Ni–Ag system. The structural refinement during HPT processing of these types of composites is characterized by strong plastic deformation in the soft phase, while the fragmentation of the hard phase is governed by elongation and repeated fracturing of the particles. If the volume fraction of the hard phase is high enough, homogenization of the composite could be obtained. The final microstructures are either nanocomposites with partial supersaturation of the phases, or full supersaturation with a single-phase structure was achieved. When the hard phase is present in a low volume fraction, the effect of strong strain localization in the soft phase is very pronounced,

leading to a retardation of the refinement process of the hard phase, as seen in Cu-26 at% Co. Second, when the hardness difference between the phases is not pronounced, as in Cu–Fe and Cu–Ag, the individual phases co-deform to lamellar structures. If one of the phases is existent in a minor volume fraction, homogeneous deformation leads to a single-phase supersaturated solid solution. If the phases exist in nearly equal volume fraction, as in the Cu-53 at% Fe composite, a nanocomposite composed of a Cu-rich and a Fe-rich phase develops. And third, systems which deform mainly by shear banding, as observed in the Cu-37 at% Ag and the Ni-35 at% Ag composites. The localized deformation prevents homogenization of the composite and inhomogeneous structures with partial supersaturation are obtained.

From the studies conducted so far, it seems that either the level of the positive heat of mixing, triggered mainly by the lattice structure and atomic radius differences, or strong variations in the mechanical properties limits the degree of supersaturation in the fcc-bcc material systems. The fcc-fcc systems are prone to shear banding in medium compositions, preventing homogenization of the composites. In the Cu–Ag system, in literature, complete supersaturation was shown also by HPT processing in medium compositions, however, with an unconstrained HPT setup in cyclic mode.[82] It is, therefore, assumed if shear banding can be suppressed at RT deformation, a full mixture of Cu and Ag is achievable.

The results indicate that the fundamental mixing mechanism leading to supersaturation is possibly not the same in the different analyzed materials systems. In the composites with a hard and a soft phase (studied in detail e.g., for Cu–Co composites), an abrasion-like process is proposed, inducing a mixing already at relatively low applied strains. The subsequent final mixing at high strains might be realized by other mechanisms (e.g., dislocation shuffling). On the other hand in the Cu–Ag system with two ductile phases, the mixing behavior in the lamellar nanocomposites indicates a mixing process by dislocations crossing phase boundaries, triggered by a critical phase dimension. However, no explicit prediction on the degree of supersaturation in a certain material system during HPT deformation can be made on the simple basis of the materials properties. Detailed studies on the deformation behavior at different stages of deformation are inevitable, especially considering the formation of shear bands and the different capabilities for plastic deformation of the individual phases.

Once the details of the microstructural evolution during HPT deformation of the composites are known, production routes to achieve the desired nanostructures and, thus, tailored properties for each possible application can be designed. There are different properties, which might be considered: structural properties like a superior combination of strength and ductility or functional properties, such as magnetic properties. In Cu–Ag composites, but also in several other nanocomposites, the optimum between strength and ductility is obtained in lamellar structures.[83,84] For applications which demand high electrical conductivity combined with high strength and ductility, the electrical conductivity – usually lowered by defects and grain boundaries – might be recovered by subsequent annealing treatments of the as-deformed composites. Further improvements might be achieved by adjusting bimodal grain or phase size distributions.[85] Other promising candidates for technical applications are HPT deformed Cu–Fe and Cu–Co composites. The magnetic properties of these materials might be modified in a wide range by decomposition of the formed supersaturated solid solutions. A production route based on HPT deformation to achieve a fully supersaturated state followed by annealing, might lead to unique nanostructures consisting of finely dispersed magnetic and non-magnetic phases. With the annealing time, the size of the magnetic phase might be tuned. With the initial composition, the volume fraction of magnetic and non-magnetic phase can be also adjusted. Furthermore, the thermal stability in the processed composites could be significantly improved.

Article first published online: December 19, 2016
Manuscript Revised: November 18, 2016
Manuscript Received: September 26, 2016

[1] Y. Ogino, T. Yamasaki, S. Murayama, R. Sakai, *J. Non. Cryst. Solids* **1990**, *117/118*, 737.
[2] E. Gaffet, C. Louison, M. Harmelin, F. Faudot, *Mater. Sci. Eng. A* **1991**, *134*, 1380.
[3] C. Gente, M. Oehring, R. Bormann, *Phys. Rev. B* **1993**, *48*, 244.
[4] K. Uenishi, K. F. Kobayashi, K. N. Ishihara, P. H. Shingu, *Mater. Sci. Eng. A* **1991**, *134*, 1342.
[5] R. Najafabadi, D. J. Srolovitz, E. Ma, M. Atzmon, *J. Appl. Phys*. **1993**, *74*, 3144.
[6] Z. Q. Li, H. Shen, L. Chen, Y. Li, B. Günther, *Philos. Mag*. **1995**, *72*, 1485.
[7] J. Xu, U. Herr, T. Klassen, R. S. Averback, *J. Appl. Phys*. **1996**, *79*, 3935.
[8] A. R. Yavari, P. J. Desré, T. Benameur, *Phys. Rev. Lett*. **1992**, *68*, 2235.
[9] J. Eckert, J. C. Holzer, C. E. Krill III, W. L. Johnson, *J. Appl. Phys*. **1993**, *73*, 2794.
[10] J. Eckert, J. C. Holzer, W. L. Johnson, *J. Appl. Phys*. **1993**, *73*, 131.
[11] E. Gaffet, M. Harmelin, F. Faudot, *J. Alloys Compd*. **1993**, *194*, 23.
[12] J. Kuyama, H. Inui, S. Imaoka, S. Nasu, K. N. Ishihara, P. H. Shingu, *Jpn. J. Appl. Phys*. **1991**, *30*, 854.
[13] C. Suryanarayana, *Prog. Mater. Sci*. **2001**, *46*, 1.
[14] Y. Li, D. Raabe, M. Herbig, P.-P. Choi, S. Goto, A. Kostka, H. Yarita, C. Borchers, R. Kirchheim, *Phys. Rev. Lett*. **2014**, *113*, 106104.
[15] J. D. Verhoeven, W. A. Spitzig, L. L. Jones, H. L. Downing, C. L. Trybus, E. D. Gibson, L. S. Chumbley, L. G. Fritzemeier, G. D. Schnittgrund, *J. Mater. Eng*. **1990**, *12*, 127.

[16] J. Bevk, J. P. Harbison, J. L. Bell, *J. Appl. Phys*. **1978**, *49*, 6031.
[17] J. D. Embury, M. A. Hill, W. A. Spitzig, Y. Sakai, *MRS Bull*. **1993**, 57.
[18] J. Freudenberger, N. Kozlova, A. Gaganov, L. Schultz, H. Witte, H. Jones, *Cryogenics* **2006**, *46*, 724.
[19] D. Raabe, K. Miyake, H. Takahara, *Mater. Sci. Eng. A* **2000**, *291*, 186.
[20] P. Gorria, D. Martínez-Blanco, J. A. Blanco, M. J. Pérez, A. Hernando, L. F. Barquín, R. I. Smith, *Phys. Rev. B* **2005**, *72*, 1.
[21] P. Gorria, D. Martínez-Blanco, R. Iglesias, S. L. Palacios, M. J. Pérez, J. A. Blanco, L. Fernández Barquín, A. Hernando, M. A. González, *J. Magn. Magn. Mater.* **2006**, *300*, 229.
[22] A. E. Berkowitz, J. R. Mitchell, M. J. Carey, A. P. Young, S. Zhang, F. E. Spada, F. T. Parker, A. Hutten, G. Thomas, *Phys. Rev. Lett*. **1992**, *68*, 3745.
[23] J. Wecker, R. von Helmolt, L. Schultz, K. Samwer, *Appl. Phys. Lett*. **1993**, *62*, 1985.
[24] H. W. Sheng, G. Wilde, E. Ma, *Acta Mater.* **2002**, *50*, 475.
[25] S. Ohsaki, S. Kato, N. Tsuji, T. Ohkubo, K. Hono, *Acta Mater.* **2007**, *55*, 2885.
[26] X. Sauvage, G. P. Dinda, G. Wilde, *Scr. Mater.* **2007**, *56*, 181.
[27] L. Ghalandari, M. M. Moshksar, *J. Alloys Compd*. **2010**, *506*, 172.
[28] M. Hosseini, N. Pardis, H. D. Manesh, M. Abbasi, D.-I. Kim, *Mater. Des*. **2016**, *113*, 128.
[29] J. S. Carpenter, S. C. Vogel, J. E. LeDonne, D. L. Hammon, I. J. Beyerlein, N. A. Mara, *Acta Mater.* **2012**, *60*, 1576.
[30] X. Sauvage, F. Wetscher, P. Pareige, *Acta Mater.* **2005**, *53*, 2127.
[31] X. Sauvage, R. Pippan, *Mater. Sci. Eng. A* **2005**, *410–411*, 345.
[32] X. Sauvage, P. Jessner, F. Vurpillot, R. Pippan, *Scr. Mater.* **2008**, *58*, 1125.
[33] X. Quelennec, A. Menand, J. M. le Breton, R. Pippan, X. Sauvage, *Philos. Mag*. **2010**, *90*, 1179.
[34] E. H. Ekiz, T. G. Lach, R. S. Averback, N. A. Mara, I. J. Beyerlein, M. Pouryazdan, H. Hahn, P. Bellon, *Acta Mater.* **2014**, *72*, 178.
[35] M. Wang, N. Q. Vo, M. Campion, T. D. Nguyen, D. Setman, S. Dillon, P. Bellon, R. S. Averback, *Acta Mater.* **2014**, *66*, 1.
[36] S. N. Arshad, T. G. Lach, M. Pouryazdan, H. Hahn, P. Bellon, S. J. Dillon, R. S. Averback, *Scr. Mater.* **2013**, *68*, 215.
[37] P. Bellon, R. S. Averback, S. Odunuga, Y. Li, P. Krasnochtchekov, A. Caro, *Phys. Rev. Lett*. **2007**, *99*, 110602.
[38] S. Odunuga, Y. Li, P. Krasnochtchekov, P. Bellon, R. S. Averback, *Phys. Rev. Lett*. **2005**, *95*, 045901.
[39] D. Raabe, S. Ohsaki, K. Hono, *Acta Mater.* **2009**, *57*, 5254.
[40] E. Ma, J.-H. He, P. J. Schilling, *Phys. Rev. B* **1997**, *55*, 5542.
[41] Z. C. Cordero, C. A. Schuh, *Acta Mater.* **2015**, *82*, 123.
[42] P. Bellon, R. S. Averback, *Phys. Rev. Lett*. **1995**, *74*, 1819.
[43] R. Pippan, S. Scheriau, A. Taylor, M. Hafok, A. Hohenwarter, A. Bachmaier, *Annu. Rev. Mater. Res*. **2010**, *40*, 319.
[44] O. Renk, A. Hohenwarter, S. Wurster, R. Pippan, *Acta Mater.* **2014**, *77*, 401.
[45] M. Hafok, R. Pippan, *Mater. Sci. Forum* **2007**, *550*, 277.
[46] B. Yang, H. Vehoff, A. Hohenwarter, M. Hafok, R. Pippan, *Scr. Mater.* **2008**, *58*, 790.
[47] R. Pippan, F. Wetscher, M. Hafok, A. Vorhauer, I. Sabirov, *Adv. Eng. Mater.* **2006**, *8*, 1046.
[48] A. Bachmaier, M. Hafok, R. Pippan, *Mater. Trans*. **2010**, *51*, 8.
[49] A. Bachmaier, M. Kerber, D. Setman, R. Pippan, *Acta Mater.* **2012**, *60*, 860.
[50] A. Bachmaier, R. Pippan, *Int. Mater. Rev.* **2013**, *58*, 41.
[51] A. Hohenwarter, A. Bachmaier, B. Gludovatz, S. Scheriau, R. Pippan, *Int. J. Mat. Res*. **2009**, *100*, 1653.
[52] H. P. Stüwe, *Adv. Eng. Mater.* **2003**, *5*, 291.
[53] K. S. Kormout, B. Yang, R. Pippan, *IOP Conf. Ser. Mater. Sci. Eng*. **2014**, *63*, 012092.
[54] K. S. Kormout, B. Yang, R. Pippan, *Adv. Eng. Mater.* **2015**, *17*, 1828.
[55] A. Bachmaier, C. Motz, *Mater. Sci. Eng. A* **2015**, *624*, 41.
[56] A. Bachmaier, M. Pfaff, M. Stolpe, H. Aboulfadl, C. Motz, *Acta Mater.* **2015**, *96*, 269.
[57] A. Bachmaier, H. Aboulfadl, M. Pfaff, F. Mücklich, C. Motz, *Mater. Charact*. **2015**, *100*, 178.
[58] A. Bachmaier, J. Schmauch, H. Aboulfadl, A. Verch, C. Motz, *Acta Mater.* **2016**, *115*, 333.
[59] A. Bachmaier, G. B. Rathmayr, M. Bartosik, D. Apel, Z. Zhang, R. Pippan, *Acta Mater.* **2014**, *69*, 301.
[60] A. Bachmaier, J. Keckes, K. S. Kormout, R. Pippan, *Philos. Mag. Lett*. **2014**, *94*, 9.
[61] I. Sabirov, R. Pippan, *Scr. Mater.* **2005**, *52*, 1293.
[62] I. Sabirov, R. Pippan, *Mater. Charact*. **2007**, *58*, 848.
[63] D. Edwards, I. Sabirov, W. Sigle, R. Pippan, *Philos. Mag*. **2012**, *92*, 4151.
[64] F. T. N. Vüllers, R. Spolenak, *Acta Mater.* **2015**, *99*, 213.
[65] K. S. Kormout, P. Ghosh, V. Maier-Kiener, R. Pippan, *J. Alloys Compd*. **2016**, doi:10.1016/j.jallcom.2016.11.085.
[66] K. Edalati, S. Toh, M. Arita, M. Watanabe, Z. Horita, *Appl. Phys. Lett*. **2013**, *102*, 181902.
[67] E. Ma, *Prog. Mater. Sci*. **2005**, *50*, 413.
[68] T. D. Shen, C. C. Koch, *Acta Mater.* **1996**, *44*, 753.
[69] Y. Ashkenazy, N. Q. Vo, D. Schwen, R. S. Averback, P. Bellon, *Acta Mater.* **2012**, *60*, 984.
[70] N. Q. Vo, J. Zhou, Y. Ashkenazy, D. Schwen, R. S. Averback, P. Bellon, *JOM* **2013**, *65*, 382.
[71] C. W. Sinclair, J. D. Embury, G. C. Weatherly, *Mater. Sci. Eng. A* **1999**, *272*, 90.
[72] N. A. Mara, I. J. Beyerlein, *J. Mater. Sci*. **2014**, *49*, 6497.
[73] A. Misra, R. G. Hoagland, *J. Mater. Sci*. **2007**, *42*, 1765.
[74] G. Veltl, B. Scholz, H.-D. Kunze, *Mater. Sci. Eng. A* **1991**, *134*, 1410.
[75] R. Z. Valiev, *Nat. Mater.* **2004**, *3*, 511.

[76] E. Ma, H. W. Sheng, J. H. He, P. J. Schilling, *Mater. Sci. Eng. A* **2000**, *286*, 48.
[77] I. Sabirov, O. Kolednik, R. Pippan, *Metall. Mater. Trans. A* **2005**, *36*, 2861.
[78] J. Z. Jiang, C. Gente, R. Bormann, *Mater. Sci. Eng. A* **1998**, *242*, 268.
[79] J. Colin, L. Thilly, F. Lecouturier, J. P. Peyrade, S. Askénazy, J. Grilhé, *Acta Mater* **1999**, *47*, 2761.
[80] N. Sridhar, J. M. Rickman, D. J. Srolovitz, *Acta Mater.* **1997**, *45*, 2715.
[81] N. Sridhar, J. M. Rickman, D. J. Srolovitz, *J. Appl. Phys.* **1997**, *82*, 4852.
[82] M. Pouryazdan, D. Schwen, D. Wang, T. Scherer, H. Hahn, R. S. Averback, P. Bellon, *Phys. Rev. B* **2012**, *86*, 144302.
[83] Y. Z. Tian, S. D. Wu, Z. F. Zhang, R. B. Figueiredo, N. Gao, T. G. Langdon, *Acta Mater.* **2011**, *59*, 2783.
[84] Y. Z. Tian, J. J. Li, P. Zhang, S. D. Wu, Z. F. Zhang, M. Kawasaki, T. G. Langdon, *Acta Mater.* **2012**, *60*, 269.
[85] K. S. Raju, V. S. Sarma, A. Kauffmann, Z. Hegedűs, J. Gubicza, M. Peterlechner, J. Freudenberger, G. Wilde, *Acta Mater.* **2013**, *61*, 228.